The "Footprint" under a Decaying Tropical Mesoscale Convective System

MARK F. GELDMEIER AND GARY M. BARNES

Department of Meteorology, University of Hawaii, Honolulu, Hawaii

(Manuscript received 22 July 1996, in final form 2 April 1997)

ABSTRACT

On 10 February 1993, during the Tropical Ocean Global Atmosphere Coupled Ocean–Atmosphere Response Experiment, the two NOAA WP-3Ds and the NCAR Electra flew under the anvil region of a decaying mesoscale convective system (MCS). Satellite and radar observations show that the MCS had a lifetime of 16 h and deep convection had essentially ceased along the leading edge at the time of sampling. The two NOAA aircraft flew at 35-m altitude over a 150 km × 300 km area to map conditions in the wake of this MCS and estimate the fluxes at the air–sea interface using the bulk aerodynamic approximation. A 20 000-km^2 area of divergence greater than 5×10^{-5} s^{-1} characterizes the wake, which is 2°C cooler and 0.5 g kg^{-1} drier than the environment. Sensible heat fluxes are three times greater and latent fluxes are double that found in the nearby undisturbed environment. These higher fluxes are to the east of the divergence center as a result of the superposition of the MCS fields on the westerly flow. Mixed-layer heights are suppressed and a surface mesolow (0.5 mb) is found more than 100 km behind the leading edge. SST is depressed nearly 0.4°C and is coincident with a divergent stress field and the coolest air in the wake. These fields demonstrate that MCSs stabilize the atmosphere at a given location long after the convective cells have either decayed or moved away. Highest surface fluxes occur in response to convective and mesoscale modification.

1. Introduction

The Tropical Ocean Global Atmosphere (TOGA) Coupled Ocean–Atmosphere Response Experiment (COARE) was designed to explore the interaction between the western Pacific warm pool and the overlying atmosphere. Satellite studies (e.g., Nakazawa 1988; Lau et al. 1991; Mapes and Houze 1993) reveal that mesoscale convective systems (MCSs) are responsible for most of the rain delivered to this warm ocean; MCSs are also the primary conduit for heat, moisture, and momentum redistribution in the tropical troposphere (e.g., Frank and McBride 1989; LeMone et al. 1984). Here we wish to focus on one aspect of the MCSs' role in the coupled system, namely, how an MCS modifies the characteristics near the interface between air and sea. We employ the flights completed on 10 February 1993 during COARE when aircraft extensively mapped conditions at 35-m altitude in and under the anvil region of a decaying MCS.

Most prior work on how an MCS modifies the tropical oceanic subcloud layer has focused on the convective-scale downdrafts emanating from cumulonimbi along the leading edge of the system (e.g., Houze 1977; Barnes and Garstang 1982; Johnson and Nicholls 1983). However, Zipser (1977), Gamache and Houze (1982), and Johnson and Nicholls (1983) show that the gentler mesoscale downdraft (10–50 cm s^{-1}), believed to be driven by evaporation of rain falling from the thick anvil (Brown 1979; Leary 1980), also plays an important role in this modification of the atmospheric mixed layer. The entrainment of the drier midlevel air into the mixed layer produces a flux divergence of moisture (Fitzjarrald and Garstang 1981b; Nicholls and Johnson 1984) that delays the recovery of the wake region (Barnes and Garstang 1982). The net effect of both downdraft types is impressive; Gaynor and Mandics (1978) used a shipboard acoustic sounder in the Global Atmospheric Research Program's (GARP) Atlantic Tropical Experiment (GATE) to show that one-third of the time the subcloud layer is recovering from the vertical transfers within MCSs or convective clouds.

Johnson and Nicholls (1983) present one of the few analyses that provides an estimate of both the magnitude and horizontal dimension of the subcloud-layer modification for one type of MCS, a squall line. Their composite view, which assumes steadiness over 9 h, shows that a squall line sampled during GATE reduces the depth, temperature, and moisture of the mixed layer; generates a divergent flow field; and enhances the sensible and latent heat fluxes at the air–sea interface for nearly 500 km behind the leading edge. In the western Pacific, Young et al. (1995) collected data in 42 convective wakes that passed over their research vessel. Their results verify that the fluxes at the air–sea interface

Corresponding author address: Prof. Gary M. Barnes, Department of Meteorology, University of Hawaii at Manoa, 2525 Correa Road, Honolulu, HI 96822.
E-mail: garyb@ua.soest.hawaii.edu

are enhanced by the cooler, drier, faster-moving downdraft air. Their work clearly demonstrates the tendency for fluxes to be elevated in and behind, not prior to, the arrival of the MCS. Jabouille et al. (1996) also note enhancements in the fluxes at the surface, especially in the areas affected by the cooler, drier, faster-moving air of the spreading downdrafts. Esbensen and McPhaden (1996) used the TOGA–TAO (tropical atmosphere ocean) buoys to argue that there is a mesoscale enhancement to the surface fluxes. This enhancement can be significant, contributing up to 30% of the total evaporation in precipitation regions. The extent and magnitude of these effects is such that the average fluxes even for the resolvable scale of a typical general circulation model (250 km) are increased.

Less is known about how an MCS affects the sea surface temperature (SST). Johnson and Nicholls (1983) did not have the observations to see if the squall line modified SST, but radiometric measurements made from aircraft during GATE did find evidence for lower SST in an area of mesoscale downdraft for a different MCS (Gautier 1978). Greenhut (1978) also found a correlation between estimated rainfall and cooler SST and argued for the importance of the cooler rain water pooling on the sea surface. Improved instrumentation allowed Young et al. (1995) to detect a slight drop of SST (0.25°C) in the wake region of MCSs intercepted in the western Pacific. Flament and Sawyer (1995) studied the effects of a heavy rain event (95 mm over 10 h) in the intertropical convergence zone and found a layer of water 7 m deep that was 0.2°C cooler than background conditions. Their budget analysis demonstrates that the temperature of the rain, which is close to the wet-bulb temperature of the air, is an important factor affecting the heat balance of the oceanic mixed layer. Cooling may result from other factors besides rain. The MCS wind field could 1) increase the sensible heat flux to the atmosphere, 2) increase mixing in the upper ocean, and 3) produce divergent surface currents and thus upwelling, if the surface stress is divergent.

A survey of the literature shows a dearth of observations that reveal the low-level kinematic, thermodynamic, and dynamic fields associated with tropical MCSs. Specifically, there is a paucity of information dealing with the wake region of the MCS. The majority of the aircraft observations are concentrated near the leading edge and usually supply only a cross section that extends a few tens of kilometers normal to this leading edge. Ship arrays are typically too large to provide useful areal data for an MCS, though ships often may provide a slice of observations normal to the leading edge of the system. Low-flying instrumented aircraft are one platform that can quickly map the effects of the MCS.

2. Objectives

Our objective is to document the ''footprint'' left by the combined effect of the convective and mesoscale downdrafts associated with an MCS sampled during COARE. In particular, we wish to focus on conditions found in the wake region, that part of the MCS well behind the leading edge where the fluxes from the sea should be warming and moistening the subcloud layer. The fields that will be produced include SST, air temperature, and specific humidity at 10 m; airflow and divergence; and pressure perturbation. The TOGA COARE bulk aerodynamic algorithm (Fairall et al. 1996) will be used to estimate stress and sensible and latent heat fluxes over an area 150 km × 300 km. Additionally, we will use a series of truncated soundings collected around this area to estimate the mixed-layer height. Aircraft radar and cloud-top temperatures from satellite will be used to determine the stage of the life cycle of the MCS and the location of the leading edge. This effort will be similar to what Johnson and Nicholls (1983) completed for a GATE squall line, but here we will assume steadiness over a shorter period (3 h), and it will be for a slower-moving and less intense MCS found over the western Pacific warm pool, not a fast-moving MCS or squall line. Our intent is that the fields will serve as a benchmark for future numerical simulations and parameterizations that address issues dealing with the coupled system. We choose the 10 February flights since it is the only mission during TOGA COARE when the aircraft performed an extensive low-level mapping of conditions beneath a decaying MCS.

3. Data collection and quality control

a. Sampling strategy

The effective range of aircraft based at Honiara, Guadalcanal, included much of the outer sounding array (Fig. 1) and areas to the south and east, the boundary being set by 3-h flight time distance (Yuter et al. 1995). The design of each day's aircraft mission was based on the extent and coverage of very cold cloud-top temperatures as determined by satellite (see Webster and Lukas 1992).

On 10 February, the two National Oceanic and Atmosphere Administration (NOAA) WP-3Ds (*NOAA-42* and *NOAA-43*) flew a square wave pattern shown in Fig. 6c. The pattern covered a domain of 1.5° latitude and 3.0° longitude and was completed in just under 3 h. Each north–south leg was flown between 35- and 45-m altitude. At the beginning and end of each of these legs, two soundings (ascent and descent) were completed to an altitude of 1200 m. The patterns of the two WP-3Ds were interwoven, making a comparison of the data between the two aircraft possible and the removal of biases especially necessary. The National Center for Atmospheric Research (NCAR) Electra also flew a square wave pattern at 3200 m, above but not coincident with the WP-3Ds, providing information underneath the anvil cloud.

The legs completed by the WP-3Ds are used to pro-

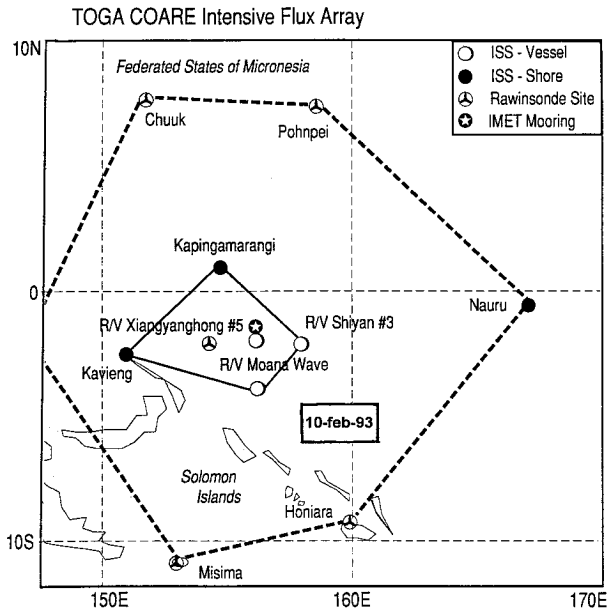

FIG. 1. The TOGA COARE intensive flux array (IFA) is the inner solid trapezoid. The outer sounding array is depicted with the dashed line. The region where the MCS in this study occurred is marked by the rectangle labeled "10-Feb-93."

duce a horizontal map of the thermodynamic, dynamic, and kinematic fields. There is, however, a major disparity in the horizontal resolution for these fields since resolution along the flight track (north–south) is governed by the sampling rate of 1 Hz (120 m), while the cross-track resolution (east–west) is a function of the spacing between aircraft legs and is about 36 km. We have elected to filter the along-track data by producing 2-min means. This effectively eliminates convective and turbulent features but retains the mesoscale gradients associated with the MCS. Our desire is to resolve the mesogamma features associated with the MCS wake.

The observations are then applied to a horizontal grid consisting of 15 × 30 grid points giving a resolution of 11 km, or 0.4 of the average distance between the input data points, which satisfies the Nyquist frequency for this distance. The grids were created using the Barnes objective analysis scheme (Barnes 1973). Some of the horizontal maps are further smoothed by subjectively removing features that were believed to be at the limit of the mesoscale resolution.

The Japanese geostationary meteorological satellite and the 5.0-cm lower fuselage radar data from the WP-3Ds were analyzed to determine the life cycle, size, evolution, and movement of the MCS. The ship-based weather radar operated continuously within the intensive flux array (IFA) but were not useful for the system being studied as the MCS stubbornly remained outside the veritable range of this radar. However, this radar imagery did aid in the analysis. Several other convective systems passed through the IFA (Fig. 1) and their radar images were compared with the satellite imagery to get a better idea of the evolution and movement of the target MCS.

b. Instrumentation and correction

The aircraft measured the horizontal wind, vertical velocity, static pressure, air temperature with both thermistors and a side-looking CO_2 radiometer, dewpoint temperature, and SST with the downward-looking PRT-5. A description of the instruments and their accuracy for the NOAA WP-3Ds can be found in Jorgensen (1984). Information on the performance of the Electra sensors during COARE is available from the NCAR Research Flight Facility. The most common problems encountered when dealing with aircraft measurements are errors in the position of the aircraft, biases in the wind velocity measurements, and sensor wetting in clouds and rain (Barnes et al. 1991).

The inertial navigation systems on the aircraft are subject to the Schuler oscillation (Fankhauser et al. 1985), as well as long-term drift. During TOGA COARE the aircraft were equipped with a global positioning system receiver that was used to verify location. The wind data were reprocessed by T. Matejka (NOAA National Severe Storms Laboratory) and adjustments were made to correct aircraft positioning. A more complete description of this reprocessing can be found in Matejka and Lewis (1997).

We use the technique of comparing reverse headings (Grossman 1977) to identify any biases in the wind direction and speed measurements. Similarly, flight legs flown by different aircraft can be compared if the temporal and spatial differences between the legs are small compared to environmental variability. Comparing the corrected wind data on similar and reverse heading legs did not uncover any biases in the wind data.

LeMone (1980) discussed the problem of measuring temperature and humidity in clouds, precipitation, or nearly saturated conditions. Flying through saturated conditions can turn the Rosemount thermometer readings into an unquantifiable wet-bulb sensor and causes spurious dewpoint readings as well. The side-looking CO_2 radiometer, which is much less affected by sensor wetting, was compared with the Rosemount thermometer. No problems were found that could be associated with sensor wetting. In fact the Johnson–Williams hot wire, which measures liquid water content, rarely responded. This sensor, though designed to sense small droplets, often will register a nonzero value in the presence of rain, too. The 10 February flights were flown well below the base of the dissipating anvil cloud, and precipitation was scattered and generally very light.

Since the data from the two WP-3Ds are combined to produce a horizontal field, systematic errors or biases between the two aircraft were of supreme concern due to the possibility of introducing artificially contrived patterns. Three methods are used to identify biases in the measurements between the two aircraft.

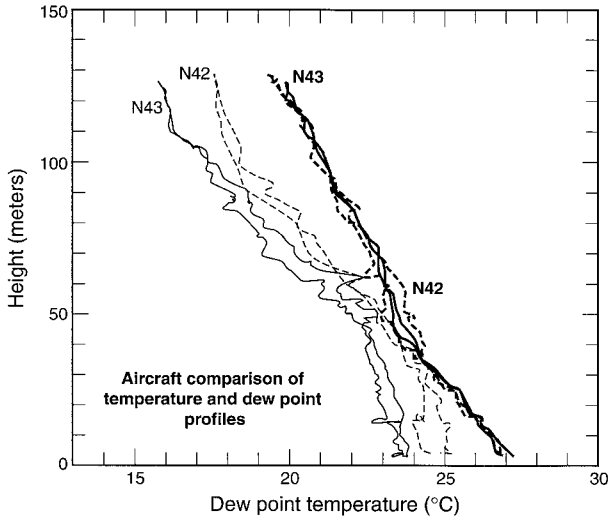

FIG. 2. Vertical profiles of temperature (°C, bold solid for *N43*, bold dashed for *N42*) and dewpoint (°C, light solid for *N43*, light dashed for *N42*) while in proximity.

The first method involves comparing measurements during takeoff and landing. At these two times the aircraft are closest in space and time. However, caution is necessary since the instruments are still feeling ''runway'' conditions at takeoff. The second method is to compare the soundings between the two aircraft. At the end of each leg, the WP-3Ds climbed from 35–45 to 1200 m, changed course, and descended to an altitude near the surface to begin the next leg. Done for obvious safety reasons during a change in heading, this also produced two ''soundings'' at each turnaround. There were several locations where the soundings from the two aircraft were in proximity. Using this method, temperature was determined not to have a bias (Fig. 2), unlike the dewpoint temperature (Fig. 2), which shows evidence of a bias of at least 1.0°C. The third method is to analyze the horizontal maps that are composed of measurements from both aircraft. A bias between the aircraft will cause any real features to be lost in a wavy pattern with the crests all correlated with one of the aircraft. As the bias is removed, the waviness fades and the mesoscale field comes into focus. Figure 3 shows a map of SST without correction for biases; Fig. 4 shows SST after the biases have been corrected.

All three methods were consistent in showing a difference in several of the measured variables between the aircraft. Once a bias was determined, a correction was applied to all of the data. The bias elimination leads to the correction of variations between aircraft, but it does not ensure the production of an accurate field. For most fields, the correction for each aircraft is one-half of the bias since it is not possible to determine which aircraft is more accurate. In the case of SST, the higher value was determined to be more likely. Both climatological means of SST and the results of several TOGA cruises suggested the warmer SST value. This was also

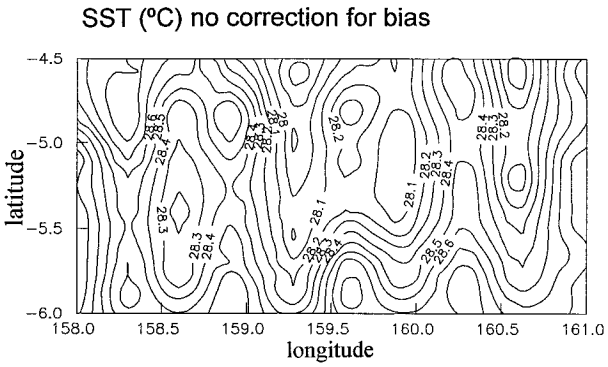

FIG. 3. Horizontal map of the radiometric SST (°C) measured by the two aircraft before any corrections are made. Contours are every 0.1°C.

supported by others (C. Friehe 1995, personal communication), who suggested that the SST from the WP-3Ds was too low.

In addition to the adjustments made for biases, the absolute value of two variables (pressure perturbation derived from D value and SST) were adjusted for other reasons. Since the aircraft pattern took place over nearly 3 h, the D-value measurements had to be adjusted for the semidiurnal pressure oscillation (Riehl 1979). The amplitude of this wave is near 1.5 mb in the region of TOGA COARE with maxima occurring at 1000 and 2200 local time. The correction during the first half of the flight is the greatest when the wave is at its steepest.

The SST, as measured by the downward-looking CO_2 radiometer, is affected by the intervening layer of air between the aircraft and the surface. Clouds and heavy rainfall in this layer make the measurement useless, while even in fair conditions there is a slight correction dependent on the temperature and humidity of this layer. By examining the change of SST during a sounding, a ''lapse rate'' could be determined following the technique of Barnes and Powell (1995). The linear correction to account for the 35–45-m layer of air in this case is +0.06° to +0.07°C, a small but clear bias to the data.

Table 1 summarizes all of the adjustments made to the data. We have not made any adjustments to the fields

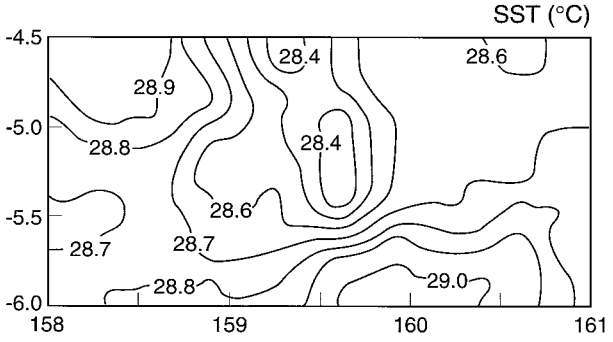

FIG. 4. Horizontal map of the radiometric SST (°C); as in Fig. 3, but after corrections have been applied.

TABLE 1. Adjustments made to WP-3D data.

Variable	*N42*	*N43*	Reason
Air temperature (°C)	+0	+0	No bias
Dewpoint temp. (°C)	−0.6	+0.6	Correction for bias
Horizontal winds (m s^{-1})	+0	+0	No bias
D value	—	—	Correct semidiurnal *P*
SST (°C)	+0.5	−0.0	Correction for bias
SST (°C)	+0.06–0.07	+0.06–0.07	Correction for altitude

in an attempt to correct for the fact that we observe the east side of the domain 3 h after we observed the west side. If during this period the fluxes are significant we might expect to find moister and warmer conditions in the east part of the domain.

c. Surface flux computation

The complete procedure used to compute the air–sea fluxes appears in Geldmeier (1996) and is the method suggested by Liu et al. (1979), with the addition of recent considerations that are used in the TOGA COARE bulk flux algorithm as presented by Fairall et al. (1996). The necessary bulk variables are gathered using the temperature from the Rosemount thermometer, SST from the downward-looking PRT-5 CO_2 radiometer, mixing ratio derived from the dewpoint measured with the General Eastern cooled mirror, horizontal and vertical winds measured as described earlier, and the altitude given by the radar altimeter. The same 2-min averages of the bulk variables that are used in the creation of the horizontal maps are also used in the bulk flux calculations. Our chief assumptions and considerations include 1) use of the wind speed rather than a resultant wind; 2) assume ocean current speed to be zero; 3) correct for the slight difference in saturated mixing ratio for the microthin layer in contact with the sea, following Sverdrup et al. (1942); 4) adjust temperature and moisture data to 10-m reference level assuming a dry adiabatic, well-mixed layer; 5) adjust flight-level measured wind speed to 10 m by using Monin–Obukhov similarity theory profiles for the near-surface layer; and 6) make transfer coefficients that are a function of a stability and a gustiness parameter (Fairall et al. 1996).

In the TOGA COARE bulk flux algorithm (Fairall et al. 1996) the neutral moisture transfer coefficient is close to 1.14×10^{-3} and has little dependence on wind speed. (Recently it has been noted that this may be even less than 1.1×10^{-3} according to Fairall, TOGA COARE 1995 flux workshop.) For unstable conditions, the algorithm increases the transfer coefficient, which increases with lighter winds. The gustiness parameter is only significant in conditions with winds under 1.5 m s^{-1}; in this study 95% of the wind speed observations were greater than 2.0 m s^{-1}. The stability parameter is dependent on wind speed also, contributing an addition of 10% to the neutral transfer coefficient at wind speeds of 7 m s^{-1} and increasing to nearly a 50% contribution with winds of 2 m s^{-1}.

The values for the heat and moisture transfer coefficients range from 1.1×10^{-3} at wind speeds of 10 m s^{-1} to 2.3×10^{-3} at wind speeds of 1 m s^{-1}. Others have found a similar range in the moisture transfer coefficient; Young et al. (1995) notes the range of 1.2×10^{-3} to 2.4×10^{-3}, which includes both undisturbed and disturbed conditions in the COARE region. Also, Bradley et al. (1991) give transfer coefficients derived from eddy-correlation measurements of 1.0×10^{-3} to 3.0×10^{-3} and show a similar dependence on wind speed.

The TOGA COARE bulk flux algorithm also includes several adjustments outside of the basic bulk flux calculations. First there is an adjustment to the SST that can be made to take into account the ''cool-skin'' effect of evaporative cooling at the interfacial layer, and the shallow ''warm layer'' of 1–2 m that results from solar heating during light wind episodes. No SST correction is necessary for SST measurements made from the radiometer, which directly measures skin temperature. The second correction is made to the latent heat flux for the ''Webb'' correction, which satisfies the need for zero dry mass flux at the surface (Webb et al. 1980). In the TOGA COARE region this would amount to an increase in the latent heat flux of 2–4 W m^{-2}. However, this addition is not made to the latent heat flux results shown in this study so that the values can be compared to previous studies.

4. Results

a. Synoptic situation

The synoptic conditions on 10 February are described in a summary from the TOGA COARE meteorological atlas (Bond and Alexander 1994). In the Northern Hemisphere, deep convection occurred in a linear pattern along a near-equatorial trough from a low at 155°E and east-southeastward through the equator at 175°E (Fig. 5). In the Southern Hemisphere, Tropical Cyclone Oliver was weakening well south of the IFA in a latitudinally aligned trough between Australia and Fiji. Along the equator, westerly winds continued and strengthened from the surface to 600 mb. Cross-equatorial flow passing through the IFA converged with the low-level westerlies, causing another band of scattered deep convec-

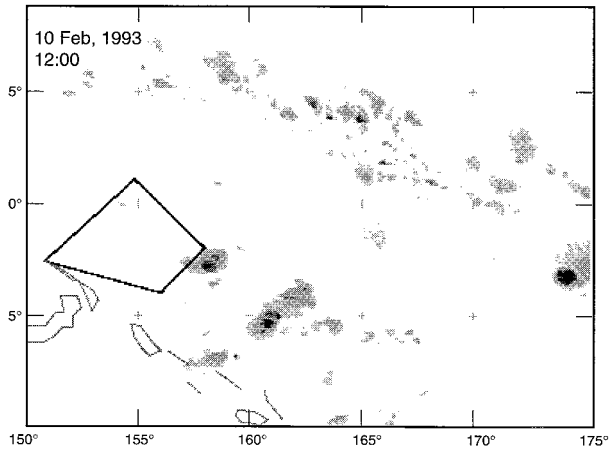

FIG. 5. Infrared satellite image at 1200 UTC 10 February 1993. The darkest shading denotes cloud-top temperatures colder than 190 K and the lightest shading denotes cloud-top temperatures colder than 208 K. Longitude (°E) and latitude (°S) are in degrees. The target MCS is located near 5°S, 161°E. The solid trapezoid is the IFA and some of the Solomon Islands are depicted by lighter solid lines.

tion from just southeast of the IFA, east toward the dateline (Fig. 5). At 200 mb, winds are easterly with a diffluent split in the flow east of the IFA.

There are no deep soundings in the region where the target MCS runs its course. Soundings to the southeast of the target MCS show a well-mixed layer to near 600 m, small dewpoint depressions in the midtroposphere, and convective available potential energy exceeding 2000 $m^2 s^{-2}$. At a height of 13 km, the temperature is near −65°C (208 K) and −83°C (190 K) at 16 km. These two temperatures will be delineated in the infrared pictures from the satellite. Winds near the surface are westerly at 6 m s^{-1} veering (Southern Hemisphere) with height and changing to easterlies by 400 mb. In the layer from 12 to 16 km, there are easterly winds of 20 m s^{-1}, showing that anvil and cirrus should blow off to the west.

b. Satellite features

Satellite data provide large-scale coverage and a context for our observations, but the coarse spatial resolution (8 km) hinders identification of overshooting tops and isolated cumulonimbi. However, outside the period of this experiment, satellite imagery may be the only tool available to observe the western Pacific warm pool region and may be the foundation for the initial conditions for numerical simulations run in real time. It is for this reason that we desire to relate our near-surface fields to satellite views of organized convection.

Cold cloud-top temperatures are related to deep convection but are not necessarily indicative of the most recent and strongest convection. The coldest cloud tops of many midlatitude mesoscale convective complexes (MCCs) produce a roughly circular shape (Maddox 1983). Our examination of tropical MCSs that move through the IFA demonstrate that linear reflectivity patterns often yield a more amorphous shape, as seen by the infrared sensors on the satellite. Both midlatitude (e.g., Smull and Houze 1985) and tropical (e.g., Zipser et al. 1981; Ishihara and Yanagisawa 1982) squall-line studies demonstrate that the linearly aligned deep convective cells produce a roughly circular shape for the cold cloud tops. Coldest cloud tops can be hundreds of kilometers behind the convective cells found along the leading edge of the MCS, suggesting that a mesoscale updraft carries the anvil cloud to colder levels. Cirrus and cirrostratus also regularly persist for many hours after the cumulonimbi that formed these clouds have dissipated.

Determining movement of an MCS from satellite is even more difficult than determining the true position of the convective cells. The cold anvil is advected by the upper-level winds. In contrast, the convergence in the boundary layer that is responsible for new cumulonimbi is driven by a different set of factors. Can one use satellite to determine MCS leading edge and its direction and speed?

Examination of several MCSs that occurred within the IFA and that were observed with both satellite- and ship-based radars lead to another technique to track propagation of the leading edge. The leading edge as defined by radar was found to be correlated with the gradient of cloud top temperature in the range of 220–240 K. This corresponds to deep convection with cloud tops higher than 9–10 km. Both radar and this temperature gradient yielded linear patterns, unlike the coldest cloud-top pattern, which would lead one to believe that the deepest convection is found in the center of a cloud cluster and exhibits no particular organization. The method filters out cloud lines composed of shallow, warm clouds as well as the slow rise of the anvil cloud that produces the coldest cloud tops well away from the new convection. Tracking the 208-K isotherm, used by Mapes and Houze (1993) to classify MCSs by their size, was found to reveal the advection of the anvil as much as it provided clues about the behavior of the leading edge. Deriving the motion of the gradient of cold cloud-top temperatures is impossible if the anvil blowoff and the leading edge move in the same direction or if there is high cloud left from previous convection that obscures the growing cumulonimbi. The reliability of tracking the gradient of cloud-top temperature increases if this feature survives for more than a few hours; direction and speed uncertainties are approximately 20° and 2 m s^{-1}.

The area of convection nearest the IFA and extending to the southeast (Fig. 5) evolved during the day with cold cloud tops merging and separating. The target system is near 5°S, 161°E, having formed around 0700 UTC. The target system at 1445 UTC contains a very large area of colder than 208-K cloud tops and even a large area of cloud tops below 190 K (Fig. 6a). However,

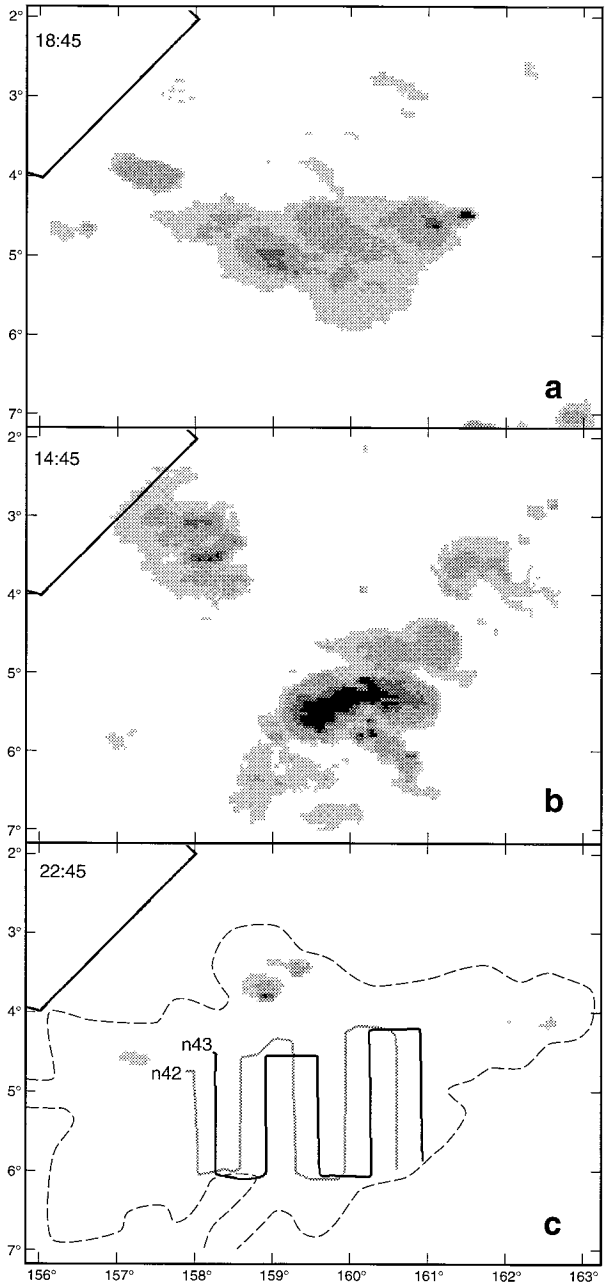

FIG. 6. Infrared satellite imagery on 10 February at (a) 1445, (b) 1845, and (c) 2245 UTC. The darkest shading denotes cloud-top temperatures colder than 190 K and the lightest shading denotes cloud-top temperatures colder than 208 K. Longitude (°E) and latitude (°S) are in degrees. The target MCS is near the center of the image. The solid angled line to the northwest is the southeastern corner of the IFA. In (c), the aircraft tracks are depicted by thin lines and a thin dashed line denotes the outline of the 220-K cloud-top temperature contour of the collapsing MCS.

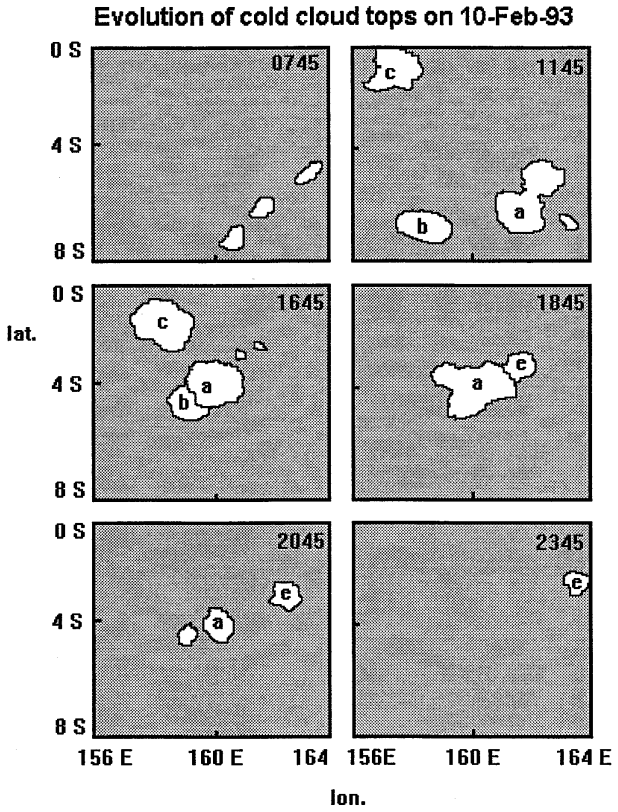

FIG. 7. Evolution of cold cloud tops on 10 February 1993 from IR satellite imagery of cloud tops colder than 208 K. The time (UTC) is given at the top right of each panel. The target MCS is labeled ''a'' and merges with ''b'' at 1645. A squall line ''c'' passes through the IFA to the northwest. Here ''e'' denotes the small squall line that forms along the northeastern edge of the target MCS.

it is at 1845 UTC that the target system reaches its maximum areal extent (60 000 km^2) based on 208 K or colder cloud tops (Fig. 6b). At this time the aircraft are just approaching the system from the south. Over the next several hours as the aircraft complete the square wave pattern (Fig. 6c), the area of 208-K cloud tops quickly diminishes. By 2245 UTC, the aircraft are leaving the system and the area of colder than 208-K cloud tops has mostly dissipated (Fig. 6c).

The evolution of these anvils is shown schematically in Fig. 7. At 0745 UTC three small areas of cold cloud tops appear to the southeast of the IFA. The middle one, designated MCS ''a,'' is the system that the aircraft fly under. At 1145 UTC a fast-moving squall line, MCS ''c'' (Fig. 7) is moving through the IFA, while MCS a continues to develop to the southeast. Over the next few hours another anvil (''b'') will move northward and merge with MCS a. The fast-moving IFA squall line (c) slows abruptly by 1645 UTC as it approaches MCS a, moving into a region that had recent convection. Some new activity appears between the two as they appear to interact. By 1845 UTC the target system is the only remaining anvil, except for a squall line (''e''), defined by its speed, that forms on the northeast edge and moves away rapidly, crossing 164°E by 2345 UTC. This squall line is much smaller and of shorter duration than the target system and though the effects of the line will be noticed in the results, it is not the focus of this study.

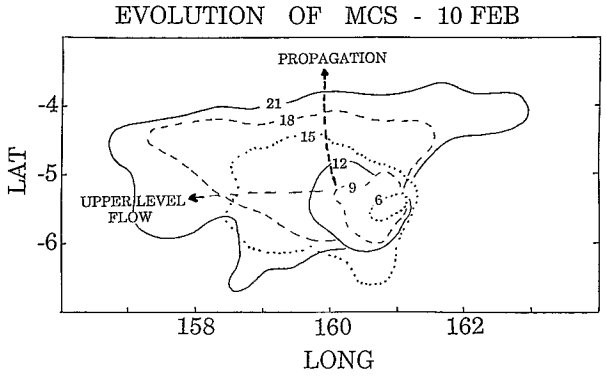

FIG. 8. Evolution of target system on 10 February 1993. The outline of the anvil is shown for various UTC. The anvil is moving with the upper flow to the west while the system is propagating northward.

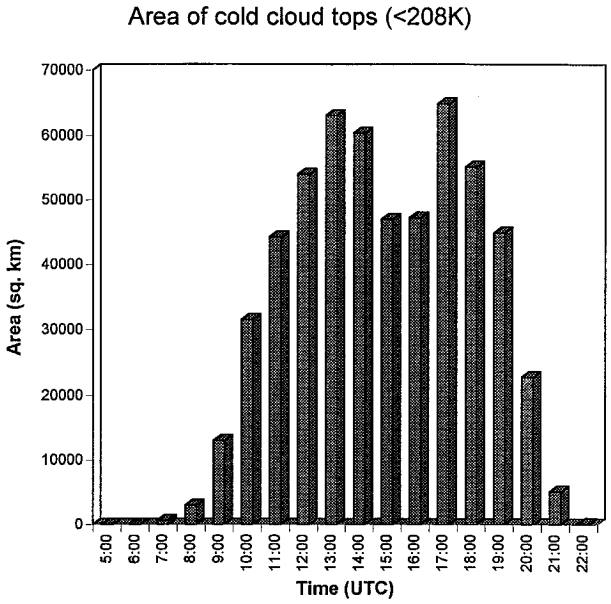

FIG. 9. Areal coverage of the 208-K or colder cloud top. The lifetime of the target MCS is 15 h and a maximum size greater than 60 000 km^2 is reached. The double peak is a result of a merging anvil from another system.

The evolution of the target MCS can be seen most clearly in Fig. 8. The easterly winds above 6 km, based on the soundings around the MCS (see Fig. 1), advect the very cold cloud-top anvil westward. However, the 220–240-K cloud-top gradient moves consistently to the north, while slowing steadily from 8 to 1 m s^{-1}. The speed decrease occurs at the same time that the overall colder than 208-K coverage diminishes and the light precipitation seen on the WP-3D radar dissipates.

Figure 9 shows the areal coverage of 208-K or colder cloud tops for the target MCS, including anvil b after the merge. The rate of both growth and decay exceed 10 000 km^2 h^{-1} with the maximum areal extent just exceeding 60 000 km^2 at 1645 UTC and remaining over 50 000 km^2 for over 6 h. With the possible exception of the eccentricity rule, this system meets the definition of an MCC (Maddox 1983). That the growing, mature, and dissipating stages cover equal expanses of time, roughly 6 h, comes as something of a surprise. Leary and Houze (1979) suggested that the convective growth stage lasts for a shorter time than the dissipating stage. It is possible that the longer mature stage might be a side effect of the merging anvils. It is estimated that the movement of the MCS from 1645 to 2245 UTC averages 7–8 m s^{-1} to the north, while the anvil advects westward at 10–15 m s^{-1}.

c. *Reflectivity structure*

Radar imagery from the lower fuselage 5-cm radar on the WP-3Ds is not available until the aircraft enter the decaying system around 1900 UTC. The individual sweeps of the radar are composited in a process described by Marks (1985) and cover a region 240 km × 240 km centered on the aircraft. The composite time of 15 min will smear the reflectivity pattern by a few kilometers given the differential speeds of the cells and the stratiform rain region. The radar image is shown overlaid on IR satellite contours (Figs. 10a,b). At 2005 UTC (Fig. 10a), there is light stratiform precipitation typical of a dissipating anvil. Reflectivity ranges from 10 dBZ up to 28 dBZ under most of the anvil, and the echoes are approximately located within the 220-K cloud-top outline. The precipitation under the decaying anvil is less than 2 mm h^{-1}, based on the Z–R relationship ($Z = 300R^{1.35}$) derived by Jorgensen and Willis (1982) for use in tropical systems. The two small convective cells in the southwest (5.5°S, between 157° and 158°E) yield much higher reflectivity of 42 dBZ (19 mm h^{-1}).

At 2105 UTC (Fig. 10b) the light precipitation is dissipating just as quickly as the 210-K anvil area dissipates. The strongest reflectivity under the anvil is near 28 dBZ (1.7 mm h^{-1}), which is similar to an average rainfall rate obtained by Gamache and Houze (1982) of 2.7 mm h^{-1} over an MCS anvil region. The remnants of the leading edge are barely visible on the northern edge of the system in both Figs. 10a and 10b. This is along the northern boundary of steep IR cloud-top temperature gradients as discussed earlier.

d. *Surface fields*

The surface field results are presented as horizontal maps that are composed of the combined in situ data from the two low-flying turboprops. The average altitude of the flight level is 38 m. The horizontal maps include an area of 55 000 km^2 from 4.5° to 6.0°S latitude and 158° to 161°E longitude, and are produced from data gathered from 1953 to 2247 UTC. The aircraft flight tracks in Fig. 6c show that there are observations at or very close to the edges of this domain. It will be seen that environmental conditions are considered to

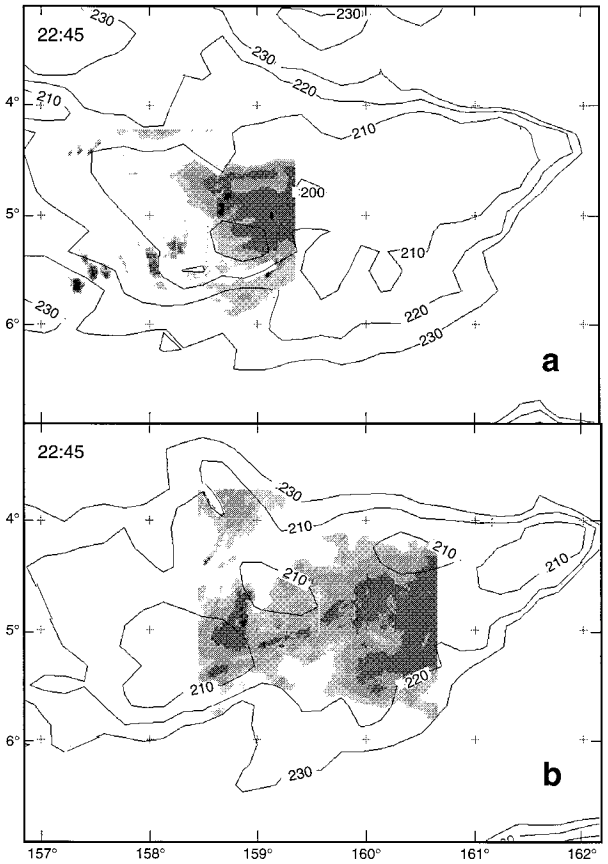

FIG. 10. Radar reflectivity at (a) 2005 and (b) 2105 UTC shown with cloud-top temperature contours derived from the GMS infrared sensors. Shadings are shown for reflectivities greater than 10, 20, 25, and 40 dBZ. The range of the aircraft radar is a rectangle of about 2° × 2°.

exist in the western quarter of the map and in the extreme south. This labeling is based on the temperature and moisture values found in the fields and how these values compare to other fair weather conditions sampled in the IFA during COARE.

The remainder of the area is considered to be the MCS wake. Active convection ended 5–8 h prior to sample time. The north central area is the last portion to be affected by the MCS leading edge, with areas to the south and east affected earlier. An exception is the extreme northeast corner, which has been modified by the recent small squall line that formed to the north of the map and moved quickly east. These various areas are summarized in Fig. 11.

The air temperature is adjusted dry adiabatically to 10 m (Fig. 12). Background values are near 28°C and the temperature is 1°–2°C cooler in the wake region. The area less than 26.5°C is over 15 000 km^2, and the coolest air temperatures are less than 26.0°C. Potential temperature (not shown), as expected, has a pattern similar to temperature. Environmental values of 300 K are depressed 1–2 K in the wake region. The temperature

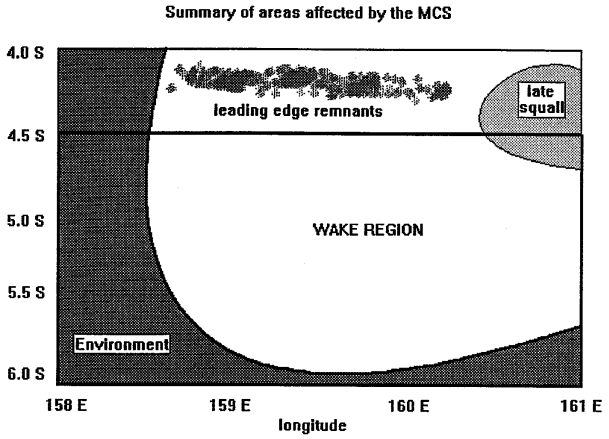

FIG. 11. The rectangle (bold), 4.5°–6.0°S and 158°–161°E, which encompasses the square wave pattern flown by the aircraft. The various areas of the MCS discussed in the text are shown. The bold rectangle is the same size as the maps of the various fields.

provides one of the strongest signals of the wake region. The steep gradient in the west is the demarcation of the wake region air interacting with environmental air. The warm air, above 28.5°C to the northwest, has probably remained convection-free longer than any other air in the environment. Warmest regions in the deep Tropics are correlated with long periods with little convective overturning (Barnes and Garstang 1982).

Environmental values of mixing ratio range from 19.0 to 19.5 g kg^{-1} (Fig. 13a). Values are drier by 0.5–1.0 g kg^{-1} in the wake region. Values of mixing ratio are more variable in the wake compared with temperature, and there is more small-scale variability. The lowest values of 16.5 are in the extreme northeast near the east side of the leading edge. Equivalent potential temperature (Fig. 13b) shows an environmental value near 358 K and wake region values depressed by 4–6 K. A low of 348 K is chiefly a result of the dry conditions; however, the wake region values varying from 348 to 356 K are a combination of both the cooler and drier air in the wake region.

The perturbation pressure field (Fig. 14) is derived

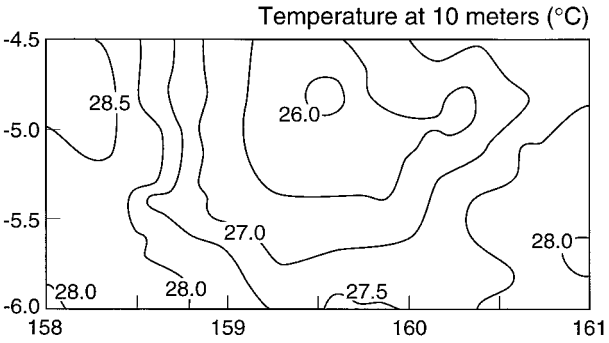

FIG. 12. Horizontal map of air temperature at 10 m. Contours are every 0.5°C. Latitude (S) and longitude (E) are in degrees.

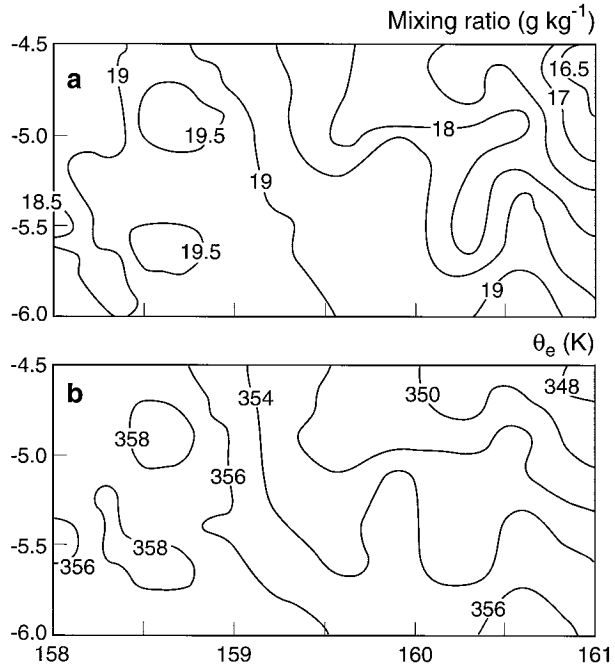

FIG. 13. Horizontal map of (a) mixing ratio and (b) equivalent potential temperature θ_e. Contours are every 0.5 g kg^{-1} and 2 K. Latitude (S) and longitude (E) in degrees.

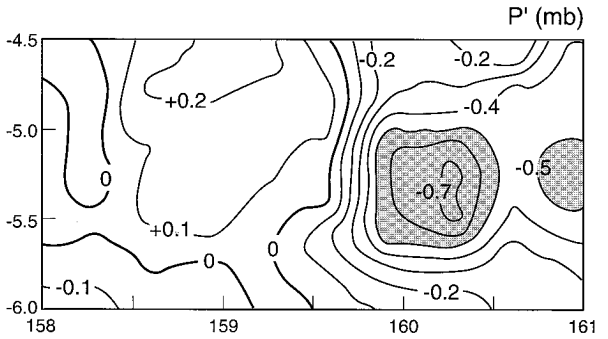

FIG. 14. Horizontal map of the pressure perturbation, which has been corrected for the semidiurnal pressure wave. Contours are every 0.1 mb. Shaded region depicts pressure perturbation lower than −0.5 mb.

using the D value, defined as the height of a given pressure surface minus the height of the same surface in a reference atmosphere. The D values are obtained from the radar altimeter and the static pressure measurements. As mentioned previously, the values have been adjusted to account for the semidiurnal pressure wave. There is a low of 0.5–0.6 mb in the center of the eastern half of the map. The low covers an area of 3000 km^2 and the gradient is steepest on the northwestern side. The position of this low is located almost 100 km behind the temperature minimum. We shall speculate on its location later in the discussion portion of the conclusions.

Winds are light in the north center and to the west (Fig. 15a). The flow becomes stronger and northerly in the south and stronger and curving westerly in the east as the air leaves the wake region. Generally the flow is diffluent in the wake region. There is some confluence where the western edge of the wake outflow boundary is interacting with the environmental flow along a north–south line (158.5° longitude). This area of confluence is also where the small active cells were indicated by the aircraft radar. Separating the wind fields into u and v components, the diffluent pattern is more apparent. The u component (Fig. 15b) shows values of 0 to −2 m s^{-1} near the confluence area, increasing steadily to the west and exceeding 7 m s^{-1}. The v component (Fig. 15c) shows values of 0 to 2 m s^{-1} at the northern part of the wake region and with some values exceeding −5 m s^{-1} on the southern edge. The increase or decrease of either component is correlated with the steep gradient of pressure (Fig. 14).

As expected, there is strong divergence in the wake region (Fig. 15d). A 20 000-km^2 area of greater than 5 × 10^{-5} s^{-1} nearly defines the wake region. In the center of the wake region, values exceed 25 × 10^{-5} s^{-1}. These values of divergence are considered to be quite significant, considering that an error in a measured wind of 1 m s^{-1} across 100 km only produces an error in divergence of 1 × 10^{-5} s^{-1}. The area of strong divergence outlines the heart of the wake region. There is convergence of −15 × 10^{-5} s^{-1} to the west, along 158.7° longitude. This coincides with a few of the weak convective cells that were present during the square wave pattern.

The average divergence can be used to estimate the strength of the mesoscale downdraft. The downdraft probably exists as high as 3–4 km and varies with height reaching a maximum of 20–40 cm s^{-1} around 3 km with much smaller values near the surface (Gamache and Houze 1982). Assuming that we have measured the average divergence in the mixed layer, we can approximate the subsidence (w_1) at the top of the mixed layer z_i by

$$w_1(z_i) = -\mathrm{DIV}z_i$$

(Stull 1988). The subsidence is in the range of 3 cm s^{-1} (5 × 10^{-5} s^{-1} and 600 m) to 5 cm s^{-1} (25 × 10^{-5} s^{-1} and 200 m), which is consistent with Gamache and Houze (1982) and Nicholls and Johnson (1984) for this level.

The corrected radiometric SST field (Fig. 4) manifests environmental or background values in the 28.8°–29.0°C range. The warmest temperatures are located in the south and there is some variation (0.3°C) in environmental SST from south to north, which is within large-scale climatological variability. In the wake region, though, values are clearly depressed by 0.2–0.4. The gradient of SST is not as sharp as some of the atmospheric variables. In the center of the wake is an area greater than 1000 km^2 that is cooler than 28.4°C. The magnitude of the cooling of SST is an order of

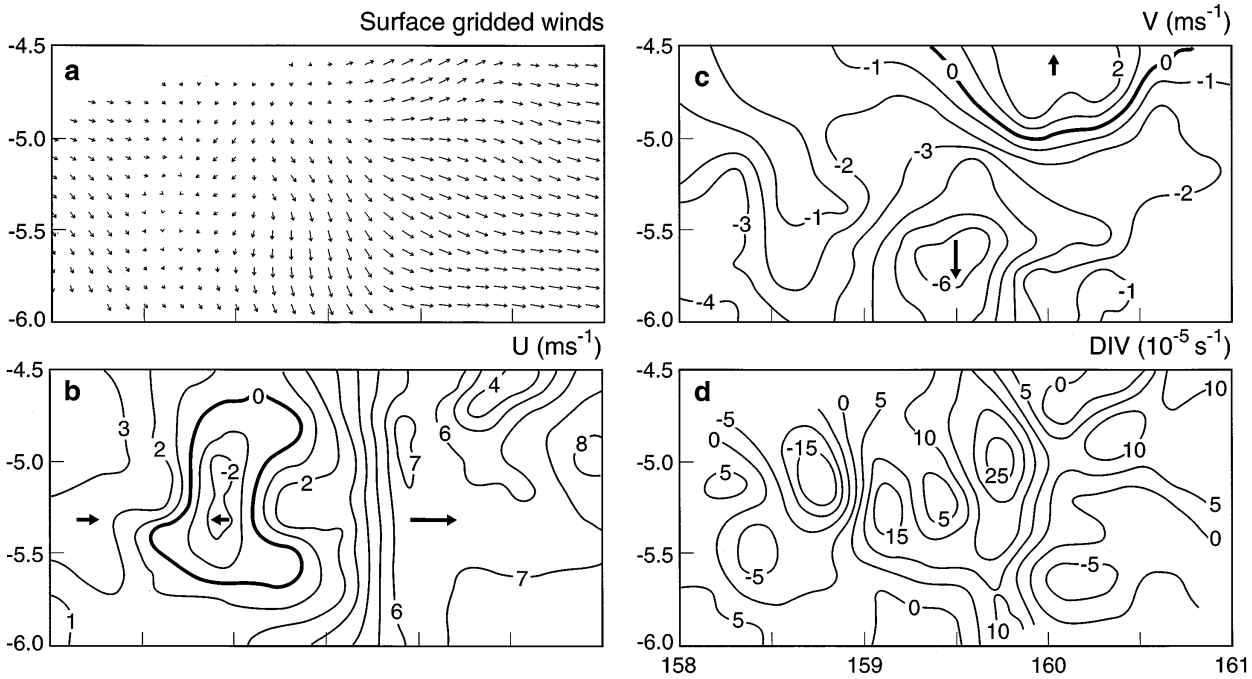

FIG. 15. Kinematic conditions at flight level: (a) horizontal flow with the maximum length shown equivalent to 9 m s^{-1}; (b) u component, (c) v component, both contoured at 1 m s^{-1}; and (d) divergence contoured at 5×10^{-5} s^{-1} increments.

magnitude less than of the air temperature, so it is mainly the drop in air temperature that drives changes in the air–sea temperature difference.

The sea–air temperature difference (Fig. 16a) of 0.5–1.0°C in the environment increases to 1.5°–2.0°C in the wake. The area of cooler air in the MCS is probably better referred to as the ''cold dome'' as opposed to the ''cold pool,'' which may be confused with the cooler SSTs. The sea–air humidity difference (Fig. 16b), where 0.98 saturation specific humidity at SST is used for surface specific humidity, shows more small-scale variability (especially on the extreme west side) and the change from the environment (~5.5 g kg^{-1}) to the wake (~6.5 g kg^{-1}) is slight. Because of the exponential dependence of saturation mixing ratio on SST, a drop of 0.5°C in the SST results in a 1.5 g kg^{-1} drop in the saturation mixing ratio. Therefore, even with drier air, changes in the air–sea humidity difference are nearly offset by the slight drop in the SST. The wind speed at 10 m is shown in Fig. 16c. In general, the wind speeds are increasing across the wake region, reaching 7 m s^{-1} by the eastern boundary. The sensible heat flux (Fig. 17a) shows environmental values of less than 5 W m^{-2}. Uncertainty in the measurements and especially the transfer coefficient would be 4–5 W m^{-2} for this environment. In the wake region there is a 7000-km^2 area of 15 W m^{-2} or greater, and the highest values exceed 20 W m^{-2}. This is an increase of 3–4 times the background value. The highest values are in the area of the greatest sea–air temperature difference along with the area where the winds are increasing. On the edges of the wake region, the values are around 10 W m^{-2} due to the increased winds.

The latent heat flux (Fig. 17b) presents a more varied pattern than the sensible heat flux. Values range from 40–80 W m^{-2} in the environment to 80–160 W m^{-2} in the wake, almost twice as high. High values on the northeast edge of the map are a result of high wind speeds and dry air from the recent squall line. Generally, values in the wake region are 1.5–2.0 times greater than the environment. The variations of sea–air humidity difference are smaller than the variations of wind speed, thus wind speed changes are the dominant factor for variations in the latent heat flux.

Wind stress (Fig. 17c) shows a pattern similar to wind speed, with values in the wake region ranging from 10 to 80×10^{-3} N m^{-2}. This is much less than what would be expected in the convective portion of the MCS. There the strongest horizontal outflows are emanating from the downdrafts, which are colocated with the high reflectivity cells.

e. Atmospheric mixed layer

A total of twenty soundings from 100- to 1200-m altitude were completed along the northern edge and southern edge of the square wave. In the tropical regions during GATE, the mixed layer averaged 500 m in undisturbed conditions and 200 m in disturbed conditions (Fitzjarrald and Garstang 1981a). Echternacht and Garstang (1976) observed no mixed layer at times or heights as low as 40 m in disturbed conditions during the Bar-

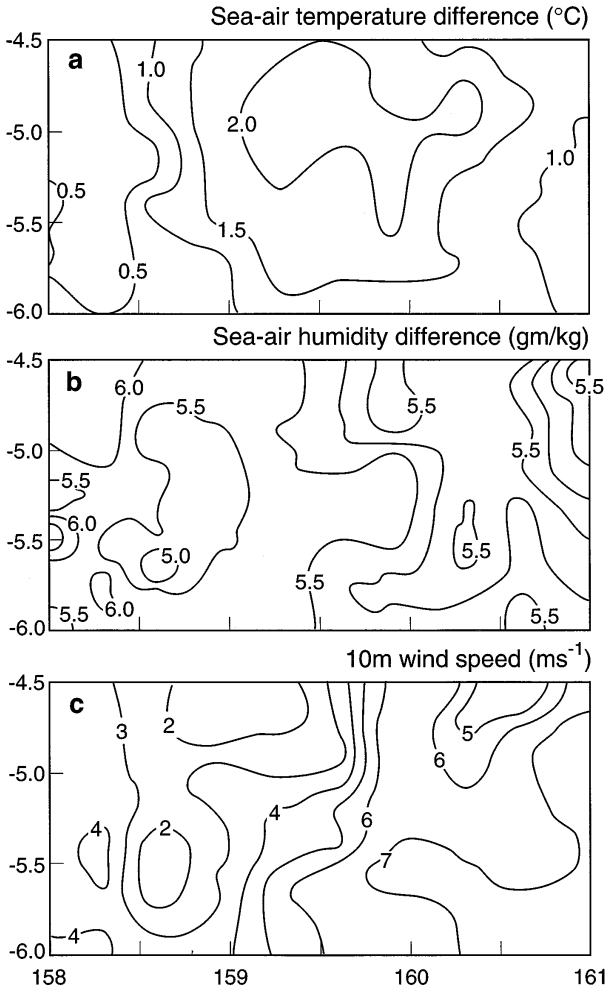

FIG. 16. Horizontal map of (a) sea–air temperature difference in 0.5°C isopleths, (b) sea–air mixing ratio difference in 0.5 g kg^{-1} isopleths, and (c) wind speed corrected to 10-m altitude in contours of 1 m s^{-1}.

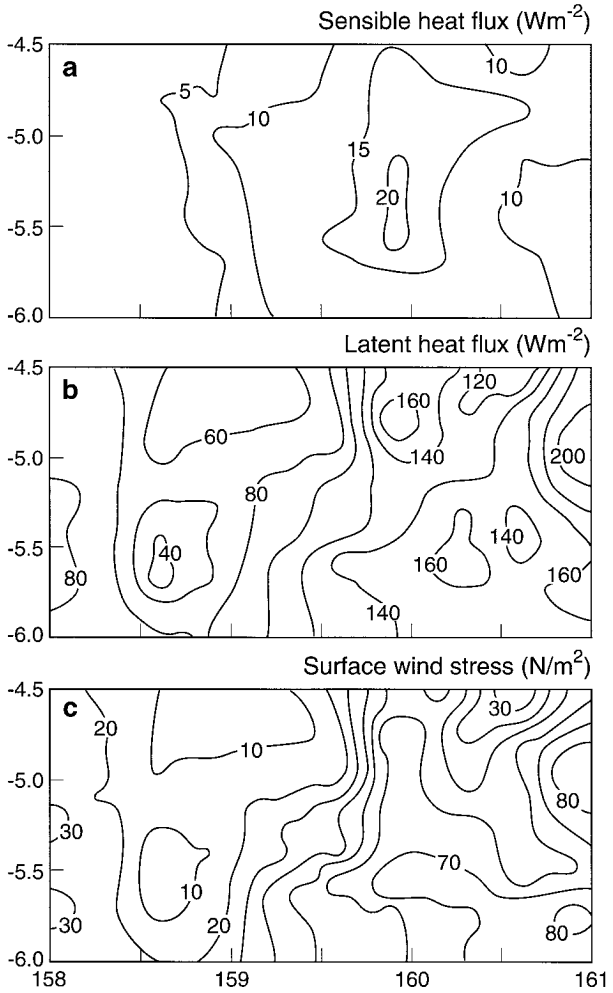

FIG. 17. Horizontal map of interfacial (a) sensible heat flux and (b) latent heat flux with contours at 5 W m^{-2} and 20 W m^{-2}, respectively; (c) wind stress, contoured at 10×10^{-3} N m^{-2}.

bados Oceanographic and Meteorological Experiment. During TOGA COARE, the mixed-layer height in undisturbed conditions is near 600 m (Young et al. 1995).

The twenty soundings were examined and a subjective twofold approach was used to determine the height of the mixed layer. In the mixed layer, the lapse rate is generally observed to be close to dry adiabatic (assuming unsaturated conditions) and the potential temperature should remain nearly constant with height. The mixed-layer height, then, is the inflection point where the potential temperature begins to increase. A second observation is that moisture is fairly well mixed in the mixed layer and then drops off sharply above. Thus, the mixing ratio or equivalent potential temperature curve can be examined to locate the height where the sounding begins to dry. In some cases this is fairly straightforward and there is high confidence in the results, but there are a few soundings that are more difficult to assess. A map of the mixed-layer heights is shown in Fig. 18. The mixed-layer height varies from 500 to 600 m in the environment and is depressed to below 200 m in the most recently disturbed part of the wake region. In general, the mixed layer is shallow in the center of the MCS

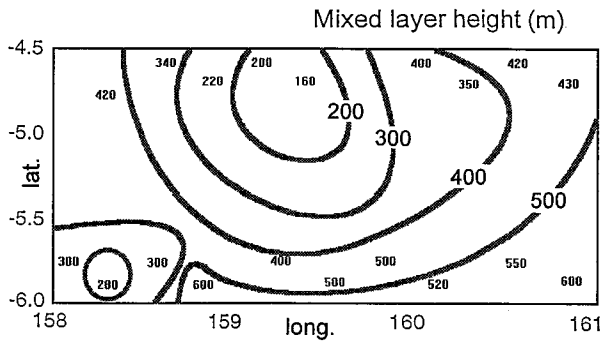

FIG. 18. Horizontal map of the mixed-layer height. Actual values are shown at the position of sounding. Contours are every 100 m.

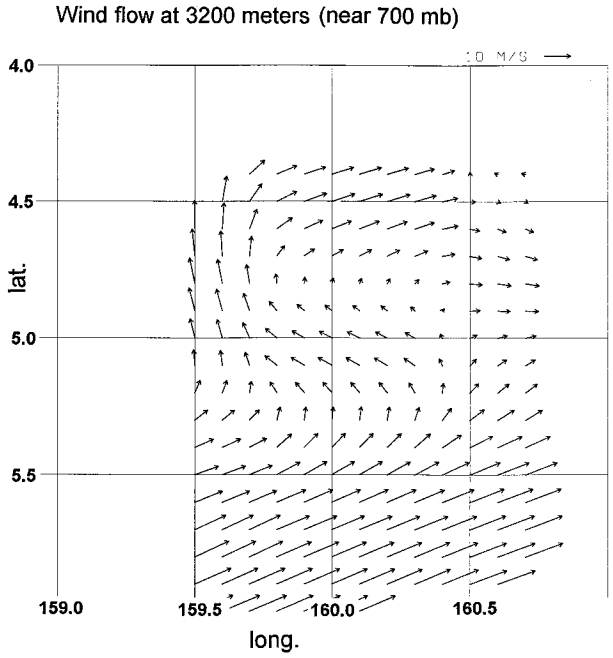

FIG. 19. Horizontal map of the wind flow at 3200 m. Cyclonic vorticity is evident. The area shown is the eastern half of the rectangle shown in the surface results. Latitude is along the left of the map and longitude along the bottom.

and is slowly rebuilding in the wake region. Both Johnson and Nicholls (1983) and Zipser (1977) observe similar depressed values of the mixed-layer height (below 200 m) in the most disturbed regions.

f. Midtroposphere structure

In addition to the two turboprops flying near the surface, the Electra flew a pattern at 3.2 km (near 700 mb), just below the anvil cloud. The pattern included three level flight legs that were about the same length as their lower altitude counterparts. The Electra track is similar to the last three legs of flight *NOAA-42* in the eastern half of Fig. 6c. Since there were only three flight legs, horizontal maps were not produced, with the exception of a map of wind flow.

The wind barbs (Fig. 19) show southwesterlies of 15 m s^{-1} in the southern half of the map, which is indicative of the background flow. In the northern half of the map, the winds appear to be curving around an area of cyclonic rotation (clockwise in the Southern Hemisphere). This ''mesovortex'' is centered around 4.75°S, 160°E with highest values of vorticity of 3×10^{-4} s^{-1}.

Johnson et al. (1989) also noted a midlevel mesovortex under a midlatitude MCS similar to the cyclonic vorticity seen here. They suggested that the mesovortex may be a consequence of the persistent surface divergence causing prolonged inflow in the midlevels and the vertical stretching enhancing background vorticity.

The potential temperature is about 1.0 K warmer at 3200 m above the surface mesolow. Most of the warming is probably occurring lower than this level, where the downdraft is likely to be stronger (Gamache and Houze 1982). However, if we assume that in the surface to 600-mb layer the average increase in virtual temperature is 1°C, the surface hydrostatic pressure change (DP) can be approximated by $DP = P\,[e^{x2} - e^{x1}]$ (Johnson et al. 1989), where $x2 = (gz_2/RT_{v2})$ and $x1 = (gz_1/RT_{v1})$, which yields a pressure change of −0.6 mb (using initial 600-mb height $z_1 = 3800$ m, final $z_2 = 3808$ m, $T_{v1} = 290$ K, $T_{v2} = 291$ K, $P = 600$ mb). This value compares well with the observations presented in Fig. 14. Johnson and Nicholls (1983) observed a warming of 1°–2°C at the 900-mb level in their study, which was associated with a surface mesolow of 2 mb.

g. Comparison to prior findings

Ship data that were collected in the same area during several TOGA COARE cruises can be used to put these results into context. The overall average of the variables in this study are compared to the cruise averages (from Fairall et al. 1996) in Table 2. The cruise means are unstratified with respect to undisturbed, active convection and wake conditions, but they do serve as an approximate check to the data correction methods used here. Both air temperature and SST are lower on 10 February, but most of the data in this study are in the wake of an MCS. The cruise means include a higher percentage of observations in undisturbed conditions.

Johnson and Nicholls (1983) show similar cooler (2°C) and drier (2 g kg^{-1}) air in the wake region with the minimum of specific humidity region trailing the air temperature minimum by up to 100 km. That the specific humidity takes longer to recover than the temperature has been discussed by Zipser (1977), Fitzjarrald and Garstang (1981a), and Nicholls and Johnson (1984).

TABLE 2. Summary of observations for this study and ship cruises in the west Pacific.

Variable	Cruise 1	Cruise 2	Cruise 3	This study
Dates of observations	11 Nov–12 Dec	16 Dec–11 Jan	28 Jan–16 Feb	10 Feb
Period of observations	22 days	26 days	18 days	3 h
Mean wind speed (m s^{-1})	3.4	5.5	4.8	4.9
SST (°C)	29.4	29.0	29.1	28.7
Air temperature (°C)	28.0	27.4	27.6	27.0
Sensible heat flux (W m^{-2})	6.6	10.9	9.6	9.7
Latent heat flux (W m^{-2})	93	119	115	114

This lag is attributed to the mesoscale downdrafts that transport warmer, drier air to the top of the recovering mixed layer in the wake region. The dry air is entrained into the deepening mixed layer, resulting in a flux divergence of moisture in that layer. Johnson and Nicholls (1983) observe a strongly divergent center in the wake region. Zipser (1977), in a discussion of the same 12 September 1974 MCS, calculated a divergence of 20×10^{-5} s^{-1} over a 10 000-km^2 area. The current study compares with a 10 000-km^2 area of 10×10^{-5} s^{-1} divergence.

Johnson and Nicholls (1983) and Zipser (1977), both studying the same squall line, observe a mesolow roughly 100 km behind the center of divergence with a magnitude of 2–3 mb. A similar mesolow is observed in this study; however, the magnitude is only 0.6 mb. The mesolow is most likely a result of a column of warm air directly above. The mesoscale downdraft adiabatically warms the air from above the mixed layer to the midtroposphere. We do not observe a mesohigh because the aircraft never flew through the northmost part of the MCS where the coolest convective downdrafts just behind the leading edge should be found. The dome of cool air is eroded farther south where the mixed layer has been undergoing recovery longer than the air found to the north of the study region.

In the MCS wake region, the sensible heat flux increases by 3–4 times and the latent heat flux increases by almost a factor of 2. Johnson and Nicholls (1983) show similar increases of nearly a factor of 5 in the sensible heat flux and a factor of 2 in the latent heat flux. The increase of the sensible heat flux is mainly due to the cooler air temperature and the latent heat flux increase, mainly due to the increased winds in both studies.

In a study of TOGA COARE convective wakes, Young et al. (1995) analyzed ship data that were affected by MCS passages to create a composite picture. The 42 convective wakes are divided into two groups, those occurring during an early pilot cruise and those that occurred during the intensive observation period (IOP) cruise. The results during the pilot cruise included MCS events that were of longer duration and greater intensity than the IOP cruise, and are more similar to the MCS in this study. The data collected from the *Wecoma* and *Moana Wave* are averaged into time bins, from 1 h before passage of the system until conditions have recovered to the prestorm values. Therefore, the first bin is representative of an environmental value, the second bin represents the convective portion, and bins 3–5 represent the wake region.

The Young et al. (1995) study for the wake region shows a decrease of air temperature (1.5°–2.0°C), a decrease of SST (0.3°C), and a decrease in mixing ratio (less than 1 g kg^{-1}). Also, the minimum mixing ratio value is seen later than the minimum air temperature. Young et al. (1995) also observe increased air–sea fluxes in the wake region, sensible heat flux increasing by 2–3 times to 20 W m^{-2}, and the latent heat flux increasing 1.5–2.0 times with values of 140 W m^{-2}. These increases are similar to what we find here.

Jabouille et al. (1996) show that MCS activity does lead to higher fluxes that can affect a large enough area to impact GCM simulations, which is verified by the spatial extent of the MCS we observe here. However, their simulation emphasizes the convective-scale outflows, not the mesoscale circulations associated with the trailing portion of the MCS that dominate the later stages of the MCS life cycle.

5. Conclusions

a. Summary

This work extends the Johnson and Nicholls (1983) GATE results of a strong, fast-moving eastern Atlantic MCS (squall line) to a slower-moving western Pacific MCS, a class-3 system based on the scheme of Mapes and Houze (1993). Satellite and radar imagery are used to describe the life cycle, size, and position of the MCS. We employ aircraft data to shorten the assumption of steadiness to 3 h, include maps of SST and wind stress, and use the latest bulk flux algorithms. This is the only case in COARE where the aircraft extensively mapped conditions at low altitudes in an MCS wake.

The cold cloud tops in the satellite imagery indicate that this MCS sampled on 10 February had a lifetime of 16 h and that the aircraft were sampling toward the end of the life cycle. Satellite imagery further showed that a small squall line formed on the northeastern edge of the aircraft pattern and moved east as the leading edge dissipated. Some of the horizontal maps show indications of this squall line; however, the results in this study concentrate on the larger mesoscale patterns associated with the decaying MCS.

Aircraft radar confirm the position of the dissipating convective leading edge to be just north of the northern edge of the aircraft pattern and that most of the remaining precipitation is light. The movement of the leading edge is determined by identifying steep cloud-top temperature gradients. The MCS movement is 7–8 m s^{-1} to the north and convection ended across the wake region ranging from 4 to 10 h prior to the sampling period. The mixed-layer environment is characterized by westerly flow of 3–4 m s^{-1}, $\theta_e \approx 358$ K, SST $\approx$ 28.8°C, and a mixed-layer height near 600 m. Together the convective- and mesoscale downdrafts produce a wake that is strongly diffluent with a 20 000 km^2 area of divergence greater than 5×10^{-5} s^{-1}; the heart of the wake region covers 1000 km^2 with divergence greater than 20×10^{-5} s^{-1}. In the wake there is a more uniform reduction of 1°–2°C in air temperature and a more variable decrease in mixing ratio of 0.5–1.0 g kg^{-1}; both lead to a 4–6-K drop in θ_e. A 0.6-mb mesolow develops that is located nearly 50 km behind the center of divergence. SST is cooled 0.2°–0.4°C over 10 000

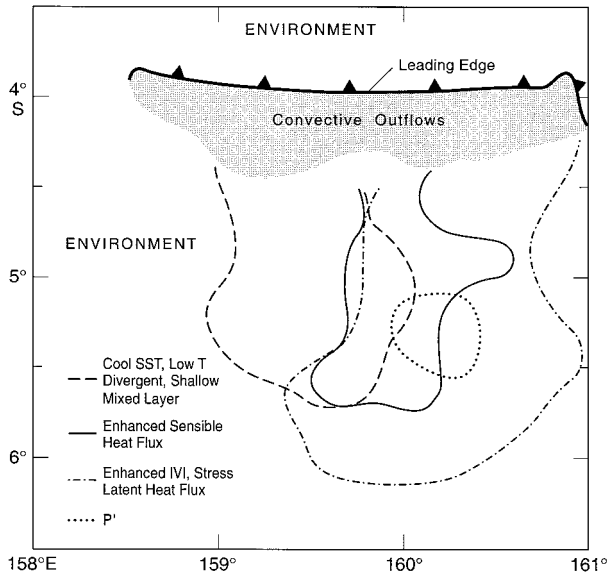

FIG. 20. Simplified horizontal map near the sea surface showing the locations of the leading edge, various overlapping fields, and the surrounding environment associated with the decaying MCS sampled on 10 February. The shading denotes convective downdrafts and outflows, and the dotted pressure perturbation (P') marks the -0.6-mb contour.

km^2. The altered wind, temperature difference, and mixing ratio difference at the air–sea interface results in an increase of the sensible heat flux by a factor of 3–4, with values exceeding 15 W m^{-2} and an increase of the latent heat flux to almost double that of the environment with an average value of 120 W m^{-2}. Stress is lowered at the center of divergence and increased toward the rear of the wake region with values approaching 0.08 N m^{-2}. The mixed-layer height is depressed below 200 m near the leading edge; the area with a mixed-layer height below 400 m is nearly 25 000 km^2.

These altered fields extend to the resolvable scale of virtually all GCMs. The increase in the sensible heat flux is primarily from the increase in the air–sea temperature difference, while the latent heat flux increase is driven more by the increased wind speeds. Confluence is apparent along the western boundary of the wake region where the wake region is interacting with the environmental flow. In the midtroposphere, cyclonic vorticity is observed above the MCS wake region. Slightly warmer temperatures observed at 3200 m above the surface mesolow support the hydrostatic explanation for the mesolow.

b. Discussion

In Fig. 20 we show a simplified depiction of the fields associated with the MCS. The leading edge is the location where there are sharp gradients in wind speed, air temperature, and moisture, all a manifestation of the downdrafts that are spreading across the sea surface. The original environmental mixed layer has been ingested by the cumulonimbi along the leading edge and there is, for a brief period of time, a layer that does not possess typical mixed-layer traits. High rain rates from the cumulonimbi along the leading edge introduce fresh, cool water to the sea. Farther behind the convective cells patterns emerge that are, initially, curious. Slightly west of the center of the line of convective cells is the first group of collocated fields. This includes the coolest SST, lowest mixed-layer heights, coolest air temperature, and strongest divergence. Skewed to the east of this first group are the wind speed, stress, and latent heat flux fields. Between this group and the first group one finds the maximum in sensible heat flux. Obviously the wind speed is the controlling factor for the collocation of the stress and latent heat flux fields, while the sensible heat flux is responding to both the difference in temperature between the sea and air and the wind speed. The minimum in pressure is southeast of the first group. Pressure is a function of what is happening throughout the troposphere; the weak low appears to be hydrostatically caused. The displacement of the flux fields to the east may be a result of the mesoscale circulation of the MCS interacting with the environmental flow. To the west the environmental flow and the divergence caused by the MCS counteract one another, while to the east the divergence is reinforcing the west to east flow.

The modified fields appear to have a smaller east–west scale than does the convection along the leading edge of the MCS. Based on the behavior of the cloud-top temperature gradient (Figs. 6 and 8), we expected to see a region exceeding 250 km in length. Instead, most of the fields of interest are about 150 km in the east–west direction. We interpret this difference to mean that under the anvil there is considerable variation in the amount of subsidence and thus the amount of forcing available to affect the recovery of the mixed layer. Strong subsidence places warm, dry air in juxtaposition with the mixed layer; this quickens the recovery of temperature but delays the recovery of the moisture. The mesoscale circulation alters the pressure and momentum fields such that two regions are produced, one with higher and the other with lower fluxes. The boundary between the modified air and the environment, given the appropriate wind regime, may also become the location for new convective development—the cells to the west are an example. Houze and Rappaport (1984) witnessed a similar effect for a GATE MCS.

This decaying MCS no longer supports convective precipitation and convective-scale downdrafts. However, underneath the anvil there remains a mesoscale downdraft. Many hours of air flowing in at the midlevels have produced a midlevel vortex. Toward the rear of the MCS, the downward motion is slowing, and this is where the 900- to 700-mb layer of air has been warmed the most. Near the surface, the center of divergence is underneath the strongest part of the mesoscale downdraft. The coolest surface air left over from convective-

scale downdrafts is found here, as well as the lowest mixed-layer height. Surface winds accelerate toward the rear of the system into the mesolow. The surface mesolow is underneath the descended, adiabatically warmed air column. The surface air is driest near the mesolow, due to mixing of warm, dry air from above.

When studying the stratiform wake region under the decaying anvil, some effects can be attributed to convective processes that have ended. The strength of these ''relics'' depends on the characteristics of the convective portion of the MCS, not the stratiform portion. However, long after convection has ceased, radar echoes have diminished, and cold cloud tops have shrunk, the wake region of the MCS persists. The size and temporal scale of the MCS wake region would cover several GCM grids with enhanced fluxes. With the cooler air temperatures, lower specific humidity, and the suppressed mixed-layer heights, convection would be limited in the wake region for many hours.

The time for recovery, that period from the initial downdraft to return to undisturbed conditions, can be different for temperature and moisture. For the temperature an estimate is possible if we know the magnitude of the cooling, the depth of this cooling, and the wind speeds at the surface. Energy inputs from the surface are dependent on the transfer coefficient, air–sea temperature difference, and wind speed. The fluxes at the top of the layer are parameterized in terms of the surface flux (Nicholls and Johnson 1984). For a column 500 m deep that is an average of 1.5°C cooler than the environment recovery will take about 10 h. We do see the mixed layer essentially returned to near-environmental conditions in about this time based on when deep convection was initially over the southernmost part of the domain.

c. SST

A decrease in SST is a function of 1) stronger mixing caused by the higher winds, 2) upwelling, 3) an increased net radiational heat loss out of the ocean due to a decrease in shortwave radiation, 4) increased latent and sensible heat fluxes, and 5) the contribution of sensible heat from raindrops. The sensible heat from raindrops, termed the ''rain heat flux'' by Flament and Sawyer (1995), is the cooling of the ocean from cold raindrops. Flament and Sawyer (1995) are concerned with heavy rainfall, 95 mm over 10 h, but even in the case of moderate rainfall, the rain heat flux has been found to be on the same order of magnitude as the increased surface sensible heat flux (Young et al. 1992). Flament and Sawyer (1995) observe the greatest net heat loss out of the ocean during the period of heaviest rain. Young et al. (1995) note that the lowest SST is observed in the period just after the convective rain ends. In this study we see the coolest SST near the ''front'' of the stratiform wake region. These three studies suggest that the greatest heat loss occurs during the convective portion of the MCS, resulting in the coolest SST just after the leading edge passes. In the MCS wake region, surface fluxes remain enhanced but increased oceanic mixing may keep the SST from decreasing any further.

SST is dependent not only on the heat loss out of the ocean, but also on the underlying structure of the oceanic mixed layer and the degree of mixing (Price et al. 1986). Changes observed in the sea surface temperature may only be a result of mixing and not heat gain or heat loss. One example could occur during periods of light winds in TOGA COARE, when very warm and shallow layers are sometimes observed. The passage of an MCS, with its accompanying strong winds, would cause an SST decrease of several degrees Celsius just because of mixing. Hence, another MCS of similar characteristics to the one in this study could produce a different SST footprint, given a different initial oceanic mixed-layer structure.

The last point of interest is a possible effect of the strong divergence occurring in the atmospheric surface layer of the MCS wake region. The area of coolest SST is closely collocated under the center of divergence. It is wondered if the period of diverging surface winds is sufficient to produce a divergent surface flow in the underlying ocean. If so, the accompanying upwelling would affect the structure of the oceanic profile as well as the SST.

Acknowledgments. This work was funded by NSF Grant ATM92-15508. We thank the NOAA and NCAR aircrews for their fine service. Dave Jorgensen, Frank Marks, Peggy LeMone, and the second author were responsible for the aircraft tactics on 10 February. We appreciate the suggestions of the two anonymous reviewers.

REFERENCES

Barnes, G. M., and M. Garstang, 1982: Subcloud layer energetics of precipitating convection. *Mon. Wea. Rev.*, **110,** 102–117.

——, and M.D. Powell, 1995: Evolution of the inflow boundary layer of Hurricane Gilbert (1988). *Mon. Wea. Rev.*, **123,** 2348–2368.

——, J. F. Gamache, M. A. LeMone, and G. J. Stossmeister, 1991: A convective cell in a hurricane band. *Mon. Wea. Rev.*, **119,** 776–794.

Barnes, S. L., 1973: Mesoscale objective map analysis using weighted time series observations. NOAA Tech. Memo. ERL NSSL-62, 60 pp. [NTIS COM-73-10781.]

Bond, G., and D. Alexander, 1994: TOGA COARE Meteorological Atlas—Bureau of Meteorology, Australia. UCAR, 366 pp. [Available from TOGA-COARE International Project Office, UCAR, P.O. Box 3000, Boulder, CO 80307.]

Bradley, E. F., P. A. Coppin, and J. S. Godfrey, 1991: Measurements of sensible and latent heat flux in the western equatorial Pacific Ocean. *J. Geophys. Res.*, **96,** 3375–3389.

Brown, J. M., 1979: Mesoscale unsaturated downdrafts driven by rainfall evaporation: A numerical study. *J. Atmos. Sci.*, **36,** 313–338.

Echternacht, K. L., and M. Garstang, 1976: Changes in the structure of the tropical subcloud layer from undisturbed to disturbed conditions. *Mon. Wea. Rev.*, **104,** 407–417.

Esbensen, S. K., and M. J. McPhaden, 1996: Enhancement of tropical

ocean evaporation and sensible heat flux by Atmospheric Mesoscale Systems, *J. Climate*, **9,** 2307–2325.
Fairall, C. W., E. F. Bradley, D. P. Rogers, J. B. Edson, and G. S. Young, 1996: Bulk parameterization of air–sea fluxes for TOGA COARE. *J. Geophys. Res.*, **101,** 3747–3764.
Fankhauser, J. C., C. J. Biter, C. G. Mohr, and R. L. Vaughan, 1985: Objective analysis of constant altitude aircraft measurements in thunderstorm inflow regions. *J. Atmos. Oceanic Technol.,* **2,** 157–170.
Fitzjarrald, D. R., and M. Garstang, 1981a: Vertical structure of the tropical boundary layer. *Mon. Wea. Rev.,* **109,** 1512–1526.
——, and ——, 1981b: Boundary-layer growth over the tropical ocean. *Mon. Wea. Rev.*, **109,** 1762–1772.
Flament, P., and M. Sawyer, 1995: Observations of the effect of rain temperature on the surface heat flux in the intertropical convergence zone. *J. Phys. Oceanogr.,* **25,** 413–419.
Frank, W. M., and J. L. McBride, 1989: The vertical distribution of heating in AMEX and GATE cloud clusters. *J. Atmos. Sci.,* **46,** 3464–3478.
Gamache, J. F., and R. A. Houze Jr., 1982: Mesoscale motions associated with a tropical squall line. *Mon. Wea. Rev.,* **110,** 118–135.
Gautier, C., 1978: Some evidence of cool surface water pooling associated with mesoscale downdrafts during GATE. *J. Phys. Oceanogr.,* **8,** 162–166.
Gaynor, J. E., and R. A. Mandics, 1978: Analysis of the tropical marine boundary layer during GATE using acoustic sounder data. *Mon. Wea. Rev.,* **106,** 223–232.
Geldmeier, M. F., 1996: Modification of the atmospheric surface layer by a decaying tropical mesoscale convective system. M.S. thesis, Dept. of Meteorology, University of Hawaii, 103 pp. [Available from Dept. of Meteorology, University of Hawaii at Manoa, 2525 Correa Road, Honolulu, HI 96822.]
Greenhut, G. K., 1978: Correlations between rainfall and sea surface temperature during GATE. *J. Phys. Oceanogr.,* **8,** 1135–1139.
Grossman, R. L., 1977: A procedure for correction of biases in winds measured from aircraft. *J. Appl. Meteor.,* **16,** 654–658.
Houze, R. A., Jr., 1977: Structure and dynamics of a tropical squall-line system. *Mon. Wea. Rev.,* **105,** 1540–1567.
——, and E. N. Rappaport, 1984: Air motions and precipitation structure of an early summer squall line over the eastern tropical Atlantic. *J. Atmos. Sci.,* **41,** 553–574.
Ishihara, M., and Z. Yanagisawa, 1982: Structure of a tropical squall line observed in the western Pacific during MONEX. *Meteor. Geophys.,* **33,** 117–135.
Jabouille, P., J. L. Redelsperger, and J. P. Lafore, 1996: Modification of the surface fluxes by atmospheric convection in the TOGA COARE region. *Mon. Wea. Rev.,* **124,** 816–837.
Johnson, R. H., and M. E. Nicholls, 1983: A composite analysis of the boundary layer accompanying a tropical squall line. *Mon. Wea. Rev.,* **111,** 308–319.
——, S. Chen, and J. J. Toth, 1989: Circulations associated with a mature-to-decaying midlatitude mesoscale convective system. Part I: Surface features—Heat bursts and mesolow development. *Mon. Wea. Rev.,* **117,** 942–959.
Jorgensen, D. P., 1984: Mesoscale and convective-scale characteristics of mature hurricanes. Part I: General observations by research aircraft. *J. Atmos. Sci.,* **41,** 1268–1285.
——, and P. T. Willis, 1982: A *Z–R* relationship for hurricanes. *J. Appl. Meteor.,* **21,** 356–366.
Lau, K.-M., T. Nakazawa, and C. H. Sui, 1991: Observations of cloud clusters hierarchies over the tropical western Pacific. *J. Geophys. Res.,* **96,** 3197–3208.
Leary, C. A., 1980: Temperature and humidity profiles in mesoscale unsaturated downdrafts. *J. Atmos. Sci.,* **37,** 1005–1012.
——, and R. A. Houze Jr., 1979: The structure and evolution of convection in a tropical cloud cluster. *J. Atmos. Sci.,* **36,** 437–457.
LeMone, M. A., 1980: On the difficulty of measuring temperature and humidity in cloud: Comments on ''Shallow convection on day 261 and mesoscale arcs.'' *Mon. Wea. Rev.,* **108,** 1702–1705.
——, G. M. Barnes, and E. J. Zipser, 1984: Momentum flux by lines of cumulonimbus over the tropical oceans. *J. Atmos. Sci.,* **41,** 1914–1932.
Liu, W. T., K. B. Katsaros, and J. A. Businger, 1979: Bulk parameterization of the air–sea exchange of heat and water vapor including the molecular constraints at the interface. *J. Atmos. Sci.,* **36,** 1722–1735.
Maddox, R. A., 1983: Large-scale meteorological conditions associated with midlatitude, mesoscale convective complexes. *Mon. Wea. Rev.,* **111,** 1475–1493.
Mapes, B. E, and R. A. Houze Jr., 1993: Cloud clusters and super clusters over the warm pool. *Mon. Wea. Rev.,* **121,** 1398–1415.
Marks, F. D., Jr., 1985: Evolution of the structure of the precipitation in Hurricane Allen (1980). *Mon. Wea. Rev.,* **113,** 909–930.
Matejka, T., and S. Lewis, 1997: Improving research aircraft navigation by incorporating INS and GPS information in a variational solution. *J. Atmos. Oceanic Technol.,* **14,** 420–433.
Nakazawa, T., 1988: Tropical super clusters within intraseasonal variations over the western Pacific. *J. Meteor. Soc. Japan,* **66,** 823–839.
Nicholls, M. E., and R. H. Johnson, 1984: A model of a tropical squall line boundary layer wake. *J. Atmos. Sci.,* **41,** 2774–2792.
Price, J. F., R. A. Weller, and R. Pinkel, 1986: Diurnal cycling: Observations of the upper ocean response to diurnal heating, cooling, and wind mixing. *J. Geophys. Res.*, **91,** 8411–8427.
Riehl, H., 1979: *Climate and Weather in the Tropics*. Academic Press, 611 pp.
Smull, B. F., and R. A. Houze Jr., 1985: A midlatitude squall line with a trailing region of stratiform rain: Radar and satellite observations. *Mon. Wea. Rev.,* **113,** 117–133.
Stull, R. B., 1988: *An Introduction to Boundary Layer Meteorology*. Kluwer Academic Publishers, 666 pp.
Sverdrup, H. U., M. W. Johnson, and R. H. Fleming, 1942: *The Oceans.* Prentice-Hall, 1087 pp.
Webb, E. K., G. I. Pearman, and R. Leuning, 1980: Correction of flux measurements for density effects due to heat and water vapor transport. *Quart. J. Roy. Meteor. Soc.*, **106,** 85–100.
Webster, P. J., and R. Lukas, 1992: TOGA COARE: The Coupled Ocean–Atmosphere Response Experiment. *Bull. Amer. Meteor. Soc.,* **73,** 1377–1416.
Young, G. S., D. V. Ledvina, and C. W. Fairall, 1992: Influence of precipitating convection on the surface energy budget observed during a Tropical Ocean Global Atmosphere pilot cruise in tropical western Pacific Ocean. *J. Geophys. Res.,* **97,** 9595–9603.
——, S. M. Perugini, and C. W. Fairall, 1995: Convective wakes in the equatorial western Pacific during TOGA. *Mon. Wea. Rev.,* **123,** 110–123.
Yuter, S. E., R. A. Houze Jr., B. F. Smull, F. P. Marks, J. R. Daugherty, and S. R. Brodzik, 1995: TOGA COARE aircraft mission summary images: An electronic atlas. *Bull. Amer. Meteor. Soc.,* **76,** 319–328.
Zipser, E. J., 1977: Mesoscale and convective-scale downdrafts as distinct components of squall line structure. *Mon. Wea. Rev.,* **105,** 1568–1589.
——, R. J. Meitín, and M. A. LeMone, 1981: Mesoscale motion fields associated with a slowly moving GATE convective band. *J. Atmos. Sci.,* **38,** 1725–1750.